Conductively coupled flexible silicon electronic systems for chronic neural electrophysiology

Jinghua Li[a,b,1], Enming Song[a,c,1], Chia-Han Chiang[d], Ki Jun Yu[e], Jahyun Koo[a,b], Haina Du[a], Yishan Zhong[a], Mackenna Hill[d], Charles Wang[d], Jize Zhang[a], Yisong Chen[a], Limei Tian[f], Yiding Zhong[a], Guanhua Fang[a], Jonathan Viventi[d], and John A. Rogers[a,b,c,g,h,i,j,k,l,m,2]

[a]Department of Materials Science and Engineering, Frederick Seitz Materials Research Laboratory, University of Illinois at Urbana–Champaign, Urbana, IL 61801; [b]Department of Materials Science and Engineering, Northwestern University, Evanston, IL 60208; [c]Center for Bio-Integrated Electronics, Northwestern University, Evanston, IL 60208; [d]Department of Biomedical Engineering, Duke University, Durham, NC 27708; [e]Department of Electrical and Electronic Engineering, Yonsei University, 03722 Seoul, Republic of Korea; [f]Beckman Institute for Advanced Science and Technology, University of Illinois at Urbana–Champaign, Urbana, IL 61801; [g]Department of Biomedical Engineering, Northwestern University, Evanston, IL 60208; [h]Department of Chemistry, Northwestern University, Evanston, IL 60208; [i]Department of Mechanical Engineering, Northwestern University, Evanston, IL 60208; [j]Department of Electrical Engineering and Computer Science, Northwestern University, Evanston, IL 60208; [k]Simpson Querrey Institute, Northwestern University, Evanston, IL 60208; [l]Feinberg School of Medicine, Northwestern University, Evanston, IL 60208; and [m]Department of Neurological Surgery, Northwestern University, Evanston, IL 60208

Contributed by John A. Rogers, August 19, 2018 (sent for review July 31, 2018; reviewed by George Malliaras and Joseph Wang)

Materials and structures that enable long-term, intimate coupling of flexible electronic devices to biological systems are critically important to the development of advanced biomedical implants for biological research and for clinical medicine. By comparison with simple interfaces based on arrays of passive electrodes, the active electronics in such systems provide powerful and sometimes essential levels of functionality; they also demand long-lived, perfect biofluid barriers to prevent corrosive degradation of the active materials and electrical damage to the adjacent tissues. Recent reports describe strategies that enable relevant capabilities in flexible electronic systems, but only for capacitively coupled interfaces. Here, we introduce schemes that exploit patterns of highly doped silicon nanomembranes chemically bonded to thin, thermally grown layers of SiO_2 as leakage-free, chronically stable, conductively coupled interfaces. The results can naturally support high-performance, flexible silicon electronic systems capable of amplified sensing and active matrix multiplexing in biopotential recording and in stimulation via Faradaic charge injection. Systematic in vitro studies highlight key considerations in the materials science and the electrical designs for high-fidelity, chronic operation. The results provide a versatile route to biointegrated forms of flexible electronics that can incorporate the most advanced silicon device technologies with broad applications in electrical interfaces to the brain and to other organ systems.

flexible electronics | neuroscience | brain interface | bioelectronics

Implantable electronic systems for electrophysiological sensing and stimulation are of increasing importance for monitoring, diagnosis, and treatment of neurological disorders (1–8). Technical requirements for electrical interfaces that offer high spatial and temporal resolution over large areas of the brain demand the use of flexible arrays of electrodes that incorporate integrated, high-performance electronics. Such platforms have the potential to allow for soft and noninvasive interfaces to the soft, curvilinear, moving surfaces of living tissues, with long-lived, stable operation while fully immersed in biofluids (9–12). The most advanced microelectrocorticography (μECoG) systems support >1,000 electrodes per square centimeter, with transistors at each node for local signal amplification and multiplexed addressing (9, 13–20), as qualitative advances over simple, passive arrays of electrodes (6, 21). Despite the appealing attributes of such systems in performance and scalability, penetration of biofluids through the interface materials (electrodes and/or encapsulation layers) into the active electronic components often occurs quickly (hours to days). The resulting parasitic pathways for current leakage and the corrosive effects on the electronic materials lead to catastrophic failure in the active components and the measurement systems, with the additional potential for damage and/or unwanted stimulation of the adjacent tissues (22–26). Recent work demonstrates that ultrathin encapsulating layers of SiO_2 derived from thermal growth on the surfaces of silicon wafers (t-SiO_2) can serve simultaneously as effective barriers to biofluids and as dielectrics for capacitive coupling to underlying electronic systems for electrophysiological sensing (27, 28). Here, the materials perfection and water impermeability of the t-SiO_2 leads to device lifetimes of many decades (estimated through accelerated testing), limited only by slow hydrolysis of the t-SiO_2 itself. Although useful in many scenarios of interest, the fundamental design requires that the capacitance between each t-SiO_2–coated sensing electrode and the surrounding tissue must be at least one order of magnitude larger than that of the capacitance associated with the gate of the corresponding sensing transistor to avoid signal attenuation (28, 29). This consideration favors decreases in the thickness of the

Significance

A critical challenge for flexible biomedical implants is in the development of materials and structures that enable intimate coupling to biotissues with long-term stability. The results presented here address this problem through a materials and integration strategy that combines highly doped silicon nanomembranes chemically bonded to thin films of thermal silicon dioxide in a construct that simultaneously serves as a biofluid barrier and a conductively coupled biointerface. Use of this approach with various flexible electronic systems, including passive and active electrodes for electrophysiological sensing and electrical stimulation, illustrate capabilities in high-fidelity operation. Systematic accelerated lifetime studies in artificial biofluids highlight the stability of these systems for chronic operation, without electrical leakage or other forms of degradation.

Author contributions: J.L., E.S., C.-H.C., K.J.Y., J.K., J.V., and J.A.R. designed research; J.L., E.S., C.-H.C., J.K., H.D., Yishan Zhong, M.H., C.W., J.Z., Y.C., L.T., Yiding Zhong, G.F., and J.A.R. performed research; J.L., C.-H.C., J.K., M.H., C.W., J.V., and J.A.R. analyzed data; and J.L., J.K., and J.A.R. wrote the paper.

Reviewers: G.M., Cambridge University; and J.W., University of California, San Diego.

The authors declare no conflict of interest.

[1]J.L. and E.S. contributed equally to this work.

[2]To whom correspondence should be addressed. Email: jrogers@northwestern.edu.

This article contains supporting information online at www.pnas.org/lookup/suppl/doi:10.1073/pnas.1813187115/-/DCSupplemental.

Published online September 18, 2018.

t-SiO_2 and increases in the sizes of the electrodes. Unfortunately, the former limits the lifetimes, while the latter limits the spatial resolution (28). Furthermore, the capacitive construction restricts capabilities in electrical stimulation. An ideal solution would provide direct electrode/tissue interfaces for conductively coupled sensing and Faradaic charge injection (30), without compromising the barrier performance of the system, to enable stable, chronic operation in a manner that can scale naturally to high levels of spatial resolution.

The following results represent a solution that exploits a unique biointerface constructed from thin, highly doped pads of silicon (silicon nanomembranes, p^{++}-Si NMs) intimately bonded to a layer of t-SiO_2. The p^{++}-Si NMs serve as electrical connections between electronics on the back of this interface structure and targeted tissues on the front, through small, aligned openings in the t-SiO_2. Here, metal electrodes patterned on the side of the t-SiO_2 opposite to the p^{++}-Si NMs form electrical contacts to surrounding tissues. A system of electronics on the other side provides active, multiplexed sensing/stimulating functionality that connects through the p^{++}-Si NMs to these electrodes. In this way, the p^{++}-Si NMs simultaneously serve as an essential part of the encapsulating structure (with the t-SiO_2) and as conductively coupled interfaces to tissues, on one side, and to the channels of silicon transistors for sensing and multiplexed addressing on the other. The intimate, chemically bonded interface between the p^{++}-Si NMs and the t-SiO_2, together with the slow rates of dissolution of these defect-free layers, yields chronically stable operation. The dual-sided geometry is critically important because it enables electrical biointerfaces at high areal coverages, independent of the area occupied by the electronics. This architecture combines the following attractive features for applications in μECoG: (*i*) conductive coupling between targeted organs and electrodes, for high-fidelity recording and/or efficient stimulation, (*ii*) multiplexed active electronics for matrix addressing and for signal amplification on a per-channel basis, (*iii*) sealed configuration for low leakage currents and chronic stability against penetration of biofluids, (*iv*) dual-sided design for maximized area for sensing/stimulating and for electronic functionality, and (*v*) thin and flexible construction for interfaces that can extend over large areas and across curved surfaces. Electrical performance assessments, dissolution tests, leakage measurements, and temperature-dependent studies reveal the key characteristics of systems with these designs. In vitro assessments demonstrate advantages over capacitively coupled alternatives, including capabilities in electrical stimulation. These concepts form the foundations for large-scale, flexible biointegrated electronic functionality for exploratory research and clinical applications related to the brain, the peripheral nervous system, the heart, and other organ systems.

Results and Discussion

Monocrystalline p^{++}-Si NMs and Integration into Flexible Electronic Platforms. Fig. 1*A* presents a schematic illustration of a fabrication sequence in which a monolithically bonded, ultrathin structure of t-SiO_2 and monocrystalline p^{++}-Si NMs serves as a sealed Faradaic electrical interface for biopotential recording and stimulation in flexible electronic platforms. The sequence begins with lithographic patterning, etching, and doping steps to create isolated islands of p^{++}-Si (concentration: 10^{20} atoms per cubic centimeter; *SI Appendix*, Fig. S1*A*) and n^{++}-Si (concentration: 10^{20} atoms per cubic centimeter, *SI Appendix*, Fig. S1*B*) in the top silicon layer of a silicon-on-insulator (SOI) substrate (Fig. 1 *A*, *I*). Subsequent processing yields n-type metal-oxide-semiconductor field-effect transistors (MOSFETs) on the SOI, where some patterned regions of the silicon serve as the conductively coupled biointerface (p^{++}-Si) and others as the semiconductor material for the back-plane transistors (n^{++}-Si) (Fig. 1 *A*, *II*, *Left*: 3D illustration; *Right*: schematic cross-section). Bonding the top side of this platform to a glass substrate coated with a thin film (13 μm) of polyimide (PI) and then eliminating the Si substrate yields an electronic system with the buried SiO_2 of the SOI wafer (i.e., t-SiO_2) on the surface (Fig. 1 *A*, *III*). Here, PI offers good thermal and chemical resistance as a bottom-side supporting layer. Removing the t-SiO_2 in small regions aligned to the p^{++}-Si islands through a combination of dry and wet etching steps exposes local areas of the p^{++}-Si (Fig. 1 *A*, *IV*, *Left*: 3D illustration; *Right*: schematic cross-section). Forming metal pads aligned with the p^{++}-Si establishes electrode interfaces with high areal coverage. Peeling the system away from the glass substrate yields a piece of flexible electronics that incorporates an array of conductively coupled electrical connections to the surrounding biological target (Fig. 1 *A*, *V*, *Left* and *Middle*: 3D illustration; *Right*: schematic cross-section). Here, the p^{++}-Si and t-SiO_2 act together as a defect-free barrier that prevents penetration of biofluids through to the back side of the system and as an interface for Faradic contact with biological tissues. In the following, we refer to these combined structures of p^{++}-Si and t-SiO_2 as p^{++}-Si // t-SiO_2.

Systematic tests demonstrate the exceptionally high effectiveness of biofluid isolation provided by the p^{++}-Si // t-SiO_2. For these studies, the thicknesses of the p^{++}-Si and t-SiO_2 are 170 nm and 1 μm, respectively. The test structure utilizes a thin film (300 nm) of Mg deposited by electron-beam evaporation (Fig. 1*B* and *SI Appendix*, Fig. S2) as a sensor for water penetration, where the rapid hydrolysis of Mg [$Mg + 2H_2O \rightarrow Mg(OH)_2 + H_2$] creates defects that can be easily detected by optical microscopy or even by simple visual inspection. Schematic illustrations and photographs of the test vehicles appear in *SI Appendix*, Fig. S2 *A* and *B*. Due to the slow dissolution of p^{++}-Si and t-SiO_2, the following experiments use elevated temperatures as a means to accelerate experiments to fall within a reasonable timeframe for studying failure-related chemical/physical processes. These temperatures also allow for comparison with previously published work on the dissolution of Si-based materials (27). As shown in Fig. 1*B*, the structure of p^{++}-Si (sheet resistance: 32 Ω/sq) and t-SiO_2 provides a stable electrical interface that also prevents penetration of PBS solution at a pH of 7.4 for 18 d under 70 °C, after which the underlying Mg dissolves quickly and in a spatially uniform manner. Similar experiments at 96 °C yield average lifetimes of 2.4 d. These timescales are consistent with rates of dissolution of p^{++}-Si obtained in separate experiments by reflectometry (MProbe; Semicon Soft) (*SI Appendix*, Fig. S3). The results suggest that p^{++}-Si // t-SiO_2 can act as an effective, defect-free water barrier with a lifetime limited by hydrolysis of the silicon, according to $Si + 4H_2O \rightarrow Si(OH)_4 + 2H_2$, without effects of water penetration through defects or interfaces. Coating a thin (200-nm-thick) layer of Pt onto the side of the p^{++}-Si in contact with PBS decreases the impedance and, at the same time, increases the average lifetime at 96 °C to 5.6 d and that at 70 °C to 35.7 d, consistent with geometrically frustrated diffusion of water through pinholes in the metal, thereby reducing the effective rate of dissolution of the silicon. Experiments using n^{++}-Si (concentration: 10^{20} atoms per cubic centimeter) show qualitatively similar results, although with higher rates of dissolution, consistent with previously reported effects of space charges on the surface on the hydrolysis reactions (31). According to this theory, p-type dopants shrink the width of the space-charge layer on the silicon surface. As a result, electrons injected into the conduction band during chemical oxidation tend to recombine with holes from the valence band, thereby impeding the reduction of water to form new hydroxide ions on the surface. Summaries of lifetimes of test devices with different encapsulation layers appear in *SI Appendix*, Fig. S4.

Electrochemical impedance spectroscopy measurements using passive electrodes formed with p^{++}-Si // t-SiO_2 provide additional information. Fig. 1*C*, *Left* and *SI Appendix*, Fig. S5*A*

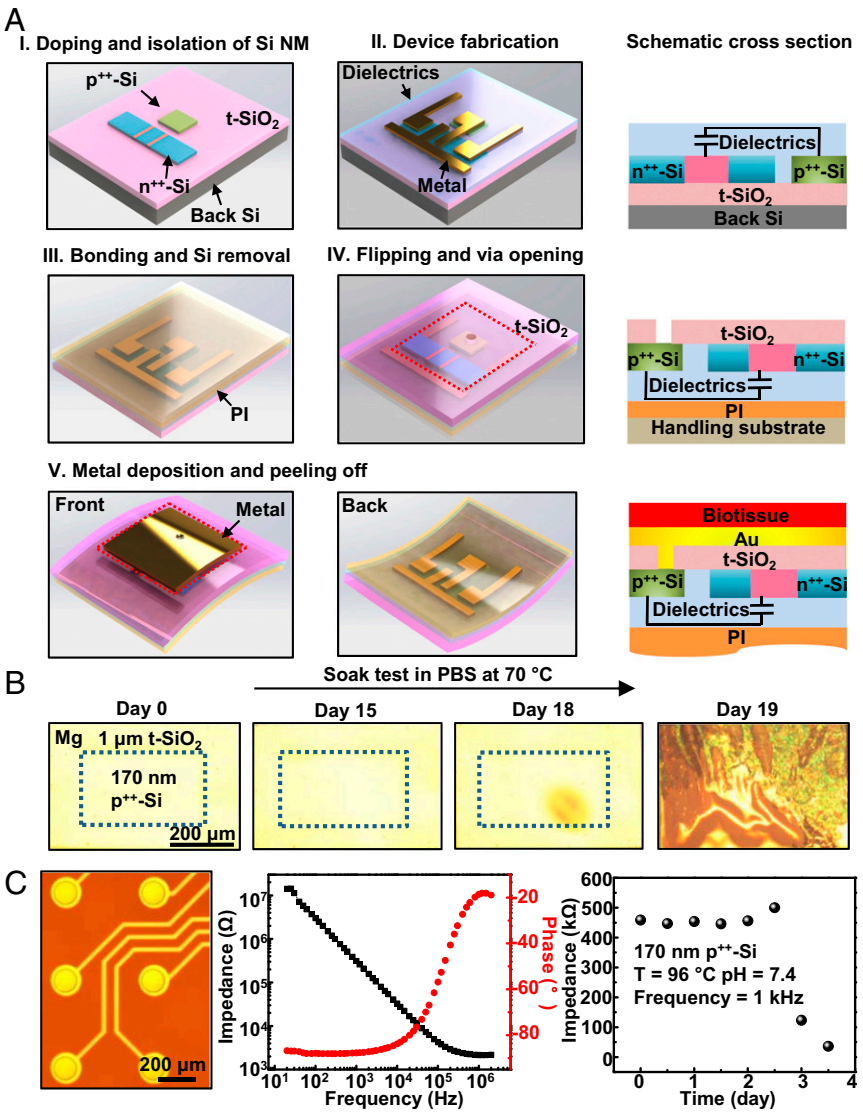

Fig. 1. Materials and integration strategies for use of monolithically bonded structures of highly doped Si NMs and thermally grown silicon dioxide (t-SiO_2) as electrical biointerfaces and biofluid barriers in flexible, biointegrated electronic systems. (*A*) Steps for forming structures of highly p-doped silicon (p^{++}-Si; boron at $10^{20}/cm^3$) as a conductive interface in a test platform: (*A*, *I*) doping and patterning regions of p^{++}-Si and n^{++}-Si on an SOI substrate; (*A*, *II*) fabricating active matrix circuits using an array of Si n-MOSFETs on the SOI; (*A*, *III*) bonding this circuit to a glass substrate coated with a film of polyimide (12 μm thick) and removing the Si wafer by dry etching; (*A*, *IV*) flipping the device over and forming "via" openings through the t-SiO_2 to locally expose the p^{++}-Si (the dashed line delineates the boundary of the unit cell); (*A*, *V*) depositing metal pads to seal the p^{++}-Si and peeling the device off from the handling substrate. (*B*) Sequence of optical images of a layer of Mg beneath a test device immersed in PBS solution (pH = 7.4) at 70 °C. The area inside of the blue rectangle corresponds to p^{++}-Si (thickness 170 nm). (*C*) Optical image of passive arrays of electrode encapsulated with p^{++}-Si (*Left*), electrochemical impedance spectra of a passive electrode (magnitude: black; phase: red) responses (*Middle*), and results of soak testing of a passive electrode in PBS at 96 °C showing that failure occurs at day 2.5 (*Right*).

present a schematic illustration and a microscope image of the device structure, respectively. An opening (diameter: 100 μm) formed through the t-SiO_2 defines an area of p^{++}-Si that connects to an electrode of gold deposited on the back side. Fig. 1*C*, *Middle* shows the magnitude of the impedance and the phase angle obtained during immersion in PBS (pH = 7.4). The impedance is initially ∼450 kΩ at 1 kHz and then decreases significantly after 3 d at 96 °C, coincident with penetration of PBS to the underlying Au electrical interconnects due to complete dissolution of the p^{++}-Si layer (Fig. 1*C*, *Right*). Statistical studies yield consistent findings (*SI Appendix*, Fig. S5*B*). Collectively, these impedance and water permeation tests firmly establish the potential of the p^{++}-Si // t-SiO_2 structure as a stable, water-impermeable platform for Faradaic biointerfaces, with relevance to electrical recording and stimulation.

Leakage Analysis in Active Electronics. Functional evaluations during immersion in PBS reveal the lifetime and operational stability of active, flexible electronic systems that exploit this interface structure. Here, each test device includes an n-type MOSFET (channel length: L_{eff} = 16 μm, width: W = 400 μm) with a p^{++}-Si // t-SiO_2 interface exposed to PBS solution on one side and electrically connected to the gate electrode of the MOSFET on the other (∼60-nm-thick device Si and 1-μm-thick SiO_2). A schematic illustration and several photographs appear in *SI Appendix*, Fig. S6. Fig. 2*A* (*Left Inset*) and *SI Appendix*, Fig. S6*A* provide top and bottom views of the transistor layout, respectively. The results of electrical testing while soaking in PBS (pH of 7.4 at 96 °C) solution confined by a well of poly(dimethylsiloxane) (PDMS; Sylgard 184, Dow Corning; *SI Appendix*, Fig. S6 *B* and *C*) are in Fig. 2 *A* and *B*. The devices have on/off ratios of ∼10^7,

mobilities of ~550 $cm^2 \cdot V^{-1} \cdot s^{-1}$, threshold voltages of ~0.75 V, and subthreshold swings of ~210 mV/dec, with stable behavior for 30 h at 96 °C. After this time period, the leakage current increases suddenly and the devices fail catastrophically (Fig. 2*A*, *Right Inset* and Fig. 2*B*, *Inset*). The lifetimes evaluated in the same manner but at 65 and 70 °C are 14 and 8 d, respectively (*SI Appendix*, Fig. S7). Similar devices with coatings of Au (thickness: 300 nm) deposited by thermal evaporation on the side of the p^{++}-Si in contact with PBS have lifetimes of 3 d at 96 °C, consistent with reduced rates of diffusion that follow from presence of the metal (Fig. 2*C*). Additional studies reveal lifetimes of 6 d at 90 °C, 14 d at 70 °C, and 50 d at 60 °C (*SI Appendix*, Fig. S8). These trends are consistent with Arrhenius scaling of the rate of dissolution of the silicon. Specifically (Fig. 2*D*) the rate for p^{++}-Si (in contact with PBS) depends exponentially on 1/T with an activation energy of 0.82 eV. Projected lifetimes for p^{++}-Si at a thickness of 60 nm without and with a coating of Au at physiological temperatures (37 °C) are 156 and 285 d, respectively, using Arrhenius scaling for extrapolation. Lifetimes in this range meet requirements for many classes of chronic neuroscience studies. The time can be extended simply by increasing the thickness of the p^{++}-Si, or by use of metal coatings with improved water barrier characteristics.

Sealed and Conductively Coupled Active Electronics. Integration of sensing electrodes of Au (300 nm) onto p^{++}-Si (60 nm) // t-SiO_2 (1 μm) yields platforms that can support arrays of silicon transistors for active matrix readout, as a class of flexible electronics with sophisticated capabilities in neural interfaces. Fig. 3*A* shows an exploded view illustration of a representative device from top to bottom. The overall system in this case consists of 64 multiplexed sensing sites (eight columns and eight rows), each with an area of 360 × 360 μm, such that the total size of the matrix is 3.2 × 3.2 mm (Fig. 3 *A* and *B* and *SI Appendix*, *Supplementary Note 1* and Figs. S9–S12). In the system used for testing (Fig. 3*C*), each site contains two transistors (channel length L_{eff} = 16 μm, width W = 80 μm, thickness = 60 nm). One serves as a multiplexer and the other as an amplifier for conductive sensing through the Au pads and their interface, via the p^{++}-Si // t-SiO_2, to the gate electrode. Here, each small opening through the t-SiO_2 to the p^{++}-Si establishes an electrical contact point to a large Au pad (360 × 360 μm) as the biointerface. As mentioned previously, the dual-sided nature of this configuration allows each pad to cover the entire area of the unit cell, independent of the size and configuration of the electronics on the opposite side. Specifically, the fill factor, as defined by the ratio of the cumulative area of the electrodes to the total area of the system, can approach values close to 100% even though the p^{++}-Si regions have a fill factor of only ~5% or less. These numbers are important because they highlight the ability to achieve both high fill factor for sensing/stimulation and, simultaneously, effective use of available area for the associated back-plane electronics. The ultimate resolution of this platform is limited only by the size of the transistor. Minimizing the size of the p^{++}-Si, and covering the total area of the unit cell on the biology side with metal for the sensing electrode enables both high fill factor (~100%) and high resolution. Optical images of a unit cell before and after coating with Au appear in Fig. 3*D*. The scanning electron microscopy image highlights the step edge between the t-SiO_2 and the adjacent p^{++}-Si in the region of the opening. The active matrix design allows measurement of biopotentials at each unit cell in a rapid time sequence for external recording with a minimal number of addressing wires (9).

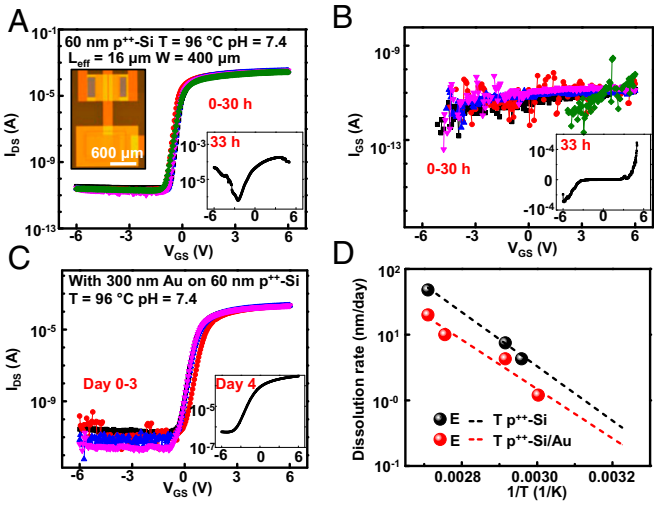

Fig. 2. Demonstration of flexible active electronics encapsulated with the p^{++}-Si // t-SiO_2 structure and analysis of leakage behaviors. (*A* and *B*) Results (subthreshold and leakage characteristics) from soak tests of a device with a p^{++}-Si via exposed to PBS solution at 96 °C. The results indicate stable operation until failure due to dissolution of the p^{++}-Si after 30 h. (*C*) Results from tests of a similar structure under identical conditions but with a coating of Au (300 nm) on the side of the system in contact with the PBS. Here, failure occurs at day 3. (*D*) Results from tests at different temperatures for structures with and without the Au coating. The lifetimes at 37 °C (156 and 285 d without and with the Au, respectively) correspond to extrapolations based on Arrhenius scaling from data collected at temperatures of 96, 70, and 65 °C for p^{++}-Si without the Au coating and of 96, 90, 70, and 60 °C for that with the Au.

Fig. 3*E* illustrates the transfer (Fig. 3*E*, *Left*, linear and log scale) and output (Fig. 3*E*, *Right*) characteristics of a test transistor fabricated together with the active matrix system on the same platform. The measurements indicate a mobility of ~600 $cm^2 \cdot V^{-1} \cdot s^{-1}$, an on/off ratio of ~$10^7$, a subthreshold swing of ~200 mV/dec, a threshold voltage of 0.7 V, and ohmic contact behavior (details appear in *Materials and Methods*). Statistics of other such transistors from 10 different samples show only minor variations in these parameters (Fig. 3*F* and *SI Appendix*, Fig. S13). Electrically biasing the PBS solution allows evaluations of the sensing capabilities of the full array and associated back-end data acquisition (DAQ) system with a Pt reference electrode (Fig. 3*G* and *SI Appendix*, Figs. S14 and S15). Fig. 3*H* shows the output characteristics of the amplifier. The sensing unit demonstrates a voltage gain (the ratio of output voltage to input voltage) of 0.99, close to the ideal value of 1 for this circuit design, as demonstrated with an alternating current (ac) signal of ~3 mV at 10 Hz. A 64-channel system with 100% yield (defined as the number of working units divided by the number of total sensing nodes) appears in Fig. 3*I*.

In Vitro Assessment of Electrical Performance. Fig. 4*A* displays histogram plots of the gain across the channels of a representative device, where the average signal magnitude (peak-to-peak) is 2.79 mV for an input of 2.8 mV at 10 Hz. The mean per-channel noise is ~37 μV (median: 33 μV) (Fig. 4*B*) and signal-to-noise ratio is 29 dB (2.8 mV) (Fig. 4*C*), with high uniformity across the system. Cumulative statistics on the average gain values and yields indicate the high levels of reproducibility and uniformity that can be achieved routinely (Fig. 4 *D* and *E*). The total leakage current of the full array system is less than 15 nA, which is comparable to the measurement noise of the DAQ system. This value falls well below levels for safe operation for a device of this size according to International Organization for Standardization standards ISO 14708–1:2014 for implantable devices (*SI Appendix*, Fig. S16).

Soak testing of completed systems at elevated temperatures yields results that are consistent with separate evaluations of materials and device components described in previous sections. When configured to limit exposure of PBS to the front sides of

ENGINEERING

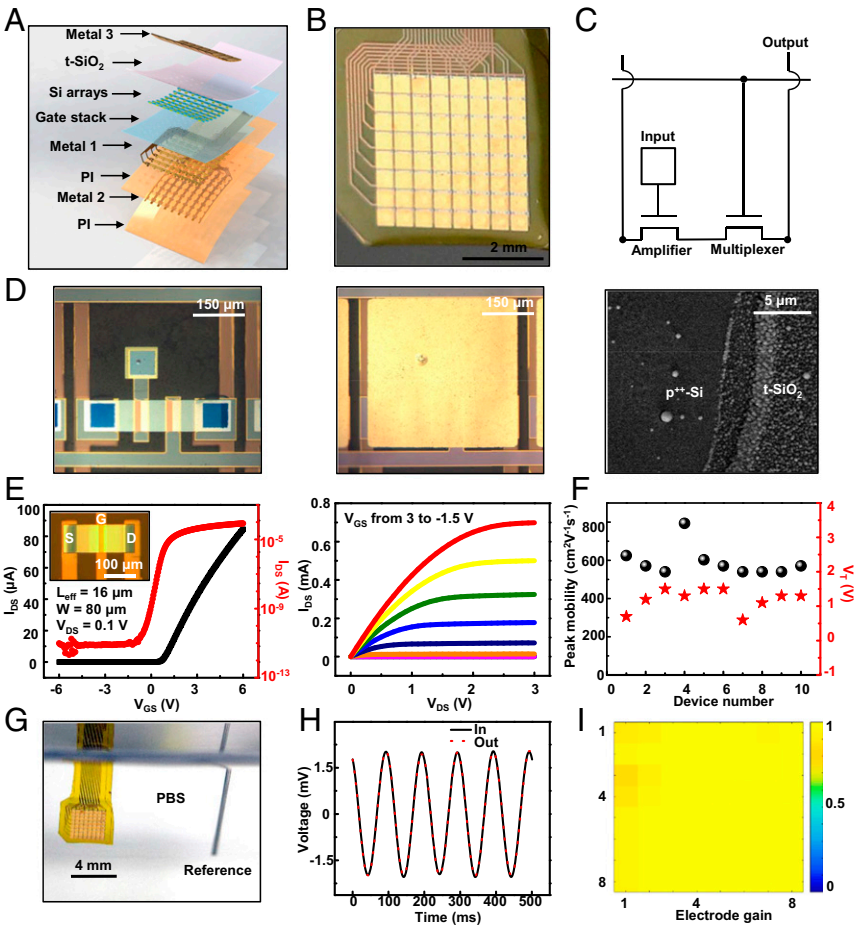

Fig. 3. Design and characterization of an actively multiplexed array of conductively coupled sensors for electrophysiological mapping, with the p^{++}-Si // t-SiO_2 structure as an interface. (*A*) Exploded view schematic illustrations of a system with 64 sensing nodes (i.e., channels). The labels highlight the different functional layers. (*B*) Photograph of a system in a slightly bent configuration. (*C*) Circuit diagram of a unit cell, with annotations for each component. (*D*) Optical microscope image of a sensing node before (*Left*) and after (*Middle*) deposition of a metal coating to define the sensing area (channel length L_{eff} = 16 μm, width W = 80 μm, thickness = 60 nm). The SEM image (*Right*) highlights the step edge between the t-SiO_2 and the p^{++}-Si in the via opening. (*E*) Transfer (*Left*) and output (*Right*) characteristics of a test transistor fabricated adjacent to the sensing matrix (*Left*, *Inset*). (*F*) Statistics of threshold voltages and peak effective mobilities of test transistors from 10 different samples. (*G*) Image of the experimental setup for the DAQ system. The device is completely immersed in PBS (pH = 7.4) at room temperature. (*H*) Output characteristics of a representative sensing node in response to an ac input of 2.8 mV at 10 Hz. (*I*) Spatial map of potential collected with a 64-channel device that has 100% yield.

the devices, the systems show stable performance in yield, gain, and noise amplitude in PBS at 96 °C until day 2.5 (Fig. 4 *F*–*H*). This lifetime is only slightly shorter than that of individual transistors (Fig. 2*C*), where the differences might be due to permeation of water through the peripheral edges of the platforms. Immersion of a Mg electrode with the interface structure in flexible form into PBS (37 °C) provides additional information about the chronic stability under conditions most similar to those for in vivo test in animal models (*SI Appendix*, Fig. S17). The device has survived for 64 d without observable changes in Mg as of when this manuscript was revised on August 10, 2018.

In vitro tests also allow evaluation of capabilities for using the p^{++}-Si as a Faradaic electrical interface for stimulation. Fig. 5*A* and *SI Appendix*, Fig. S18 show the circuit diagram and a photograph of a system of stimulation electrodes encapsulated with p^{++}-Si (170 nm) // t-SiO_2 (1 μm) in flexible form. Measurements indicate that the voltages at the p^{++}-Si electrodes are comparable to those applied at the terminal pads of metal interconnect traces (10 V, 20 Hz, 0.01 duty cycle), as expected based on electrical continuity of the traces and low-resistance contacts to the p^{++}-Si as shown in Fig. 5*B*. Studies of electrochemical stability of electrical interface materials follow published procedures for pulsed-mode operation at field amplitudes of 1–5 V/cm, pulse durations of 0.25–10 ms, and frequencies of 1–5 Hz (32–35). This mode of stimulation can result in irreversible Faradaic reactions, along with delamination and dissolution of conventional thin-film metal electrodes that use Au, Pt, Pt/Ir, or other standard materials. For example, Au forms soluble gold chloride complexes in the presence of an electric potential (1.35–1.85 V) and a small amount of chloride ion (0.001–10 mol/L) in the surrounding solution ($Au + 4Cl^- \rightarrow AuCl_4^- + 3e^-$) (36, 37). Electrodes of Pt can also form soluble complexes in saline solutions during pulsed electrical stimulation ($Pt + 4Cl^- \rightarrow PtCl_4^{2-} + 2e^-$) (38, 39). Systematic studies using continuous direct current stimulation applied to p^{++}-Si electrodes with an area of 3 × 3 mm^2 and Au electrodes with identical geometries yield comparative data on the dissolution behaviors and operational stability, with conditions relevant to clinical protocols in neural and cardiac systems. Fig. 5*C* shows the impedance spectra of p^{++}-Si immersed in PBS (pH = 7.4) before and after 12-h stimulation, as equivalent to established procedures for brain stimulation (200-μs duration, 50 Hz) for ∼1,200 h (40), with a voltage pulse of 5 V. The absence of a significant change in impedances highlights the stability of this system. By contrast, the Au electrode gradually dissolves and delaminates

(*SI Appendix*, Fig. S19), leading to a sudden increase in impedance after 6 h, consistent with failures due to the complete dissolution (Fig. 5*C*, *Inset*). Fig. 5*D* summarizes the changes in impedance at 1 kHz, highlighting the lifetimes of p^{++}-Si and Au at different voltage inputs. The lifetimes of Au evaluated in this manner for stimulation at 2, 3, and 5 V are 6 h, 2 h, and 5 min, respectively. Similarly, a 300-nm-thick Pt electrode with the same geometry also shows delamination after 30 min at 5 V. In contrast, the p^{++}-Si electrode shows no change even at 5 V for 24 h, indicating the excellent properties of this material as both an electrical interface and encapsulation layer for stimulation electrodes.

Conclusions

In summary, the results presented here provide a materials strategy and integration scheme that enables flexible, long-lived, and multiplexed active implants for Faradaic electrophysiological mapping and stimulation, with applicability across a range of various clinical and research modes of use. Systematic studies reveal that the sealed, monolithic p^{++}-Si // t-SiO_2 structure enables chronic stability and conductive coupling to biotissues simultaneously. Compatibility with state of the art electronics, including those that can be sourced from modern semiconductor foundries, is a key advantage. The dual-sided geometry allows scaling to small electrodes at high area fill factors, with geometric layouts that do not depend on the area coverage of the supporting electronics (41, 42). Mechanically flexible platforms of this sort offer many advantages compared with alternative systems for electrophysiology, with potential uses in neuroscience, cardiac science, and other areas. Immediate opportunities for further improvement are development of materials alternatives to p^{++}-Si that do not react with biofluids, as a route toward extended operating lifetimes.

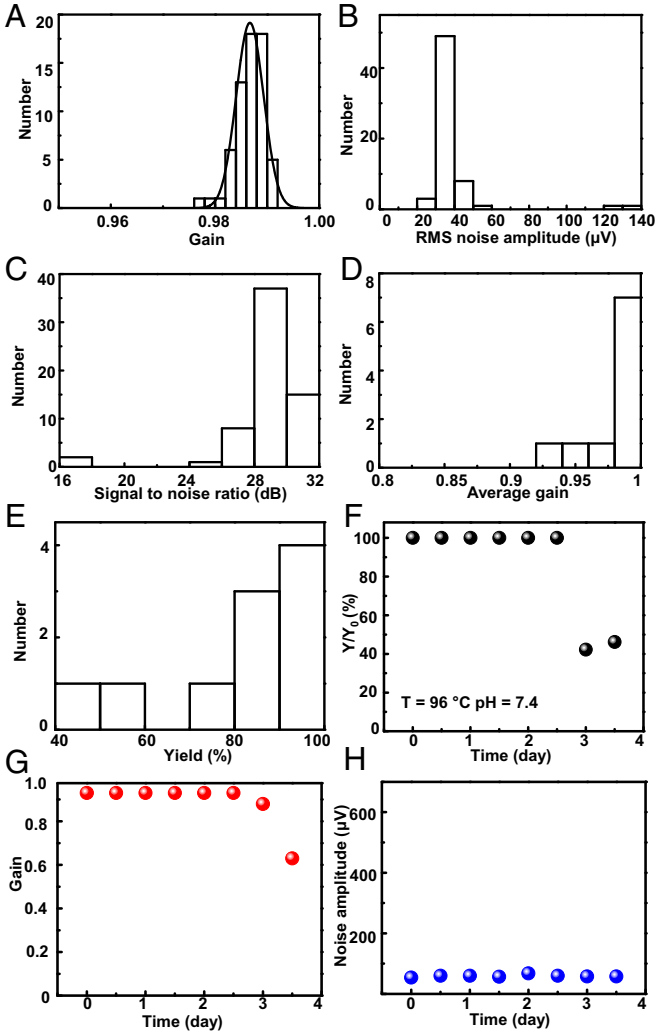

Fig. 4. In vitro measurements of the electrical performance of a conductively coupled sensing array with active multiplexed addressing. (*A–C*) Histogram of gain, noise, and signal-to-noise ratio associated with the 64 sensing nodes of a typical device. (*D* and *E*) Cumulative statistics of average gain and yield for 10 different systems of this type. (*F–H*) In vitro results from soak tests in PBS (pH = 7.4) at 96 °C, including yield, average gain, and noise amplitude. The performance remains stable until day 3, likely due to penetration of water through the perimeter edges of the system.

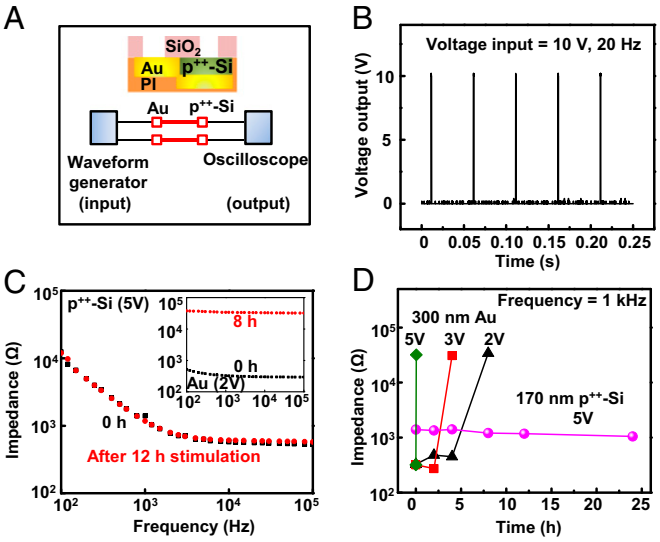

Fig. 5. In vitro assessment of the efficiency and stability of stimulation electrodes of p^{++}-Si and comparisons to otherwise similar electrodes formed with thin films of Au. (*A*) Circuit diagram of the test system with annotations for each component. (*B*) Voltage output for input pulses of 10 V (20 Hz). (*C*) Impedance spectra of a p^{++}-Si electrode and a Au electrode before and after stimulation. (*D*) Data that illustrate the lifetimes of a p^{++}-Si electrode and a Au electrode operated at different simulation voltages.

Materials and Methods

Procedures for Fabricating the Devices. Fig. 1*A* and *SI Appendix*, Fig. S10 summarize the steps for device fabrication. First, back-grinding the silicon handle of a p-type SOI wafer (200-nm device Si, 1-μm buried oxide (BOX) layer, 500-μm handle wafer; Soitec) reduced its thickness to 200 μm. Thermal oxidation at 1,150 °C in a tube furnace yielded a layer of SiO_2 (~200 nm) as a diffusion mask on the device Si. Photolithographically patterned removal of SiO_2 by reactive ion etching (RIE) with CF_4/O_2 and buffered oxide etching (BOE) defined regions for p-type doping. Thermal diffusion of boron occurred at 1,000 °C in a tube furnace to form p^{++}-Si as a conductive interface to metal electrodes. A second diffusion mask of SiO_2 deposited by plasma-enhanced chemical vapor deposition and patterned in a similar manner followed by thermal diffusion doping with phosphorus at 1,000 °C defined the source, drain, and channel regions of the transistors. Photolithography and RIE with SF_6 yielded isolated islands for n-type metal-oxide-semiconductor transistors. Thermal oxidation in a tube furnace at 1,150 °C for 15 min followed by atomic layer deposition (ALD) yielded a gate dielectric stack of SiO_2 (50 nm thick) and Al_2O_3 (13 nm thick). Immersion in BOE created openings in the SiO_2 with geometries defined by photolithography. Electron-beam evaporation formed a bilayer of 10 nm Cr/300 nm Au. Photolithography and wet etching yielded source/drain interconnects and electrical contact between p^{++}-Si and the gate electrode as the first metal layer. A thin film of polyimide (PI; 1.6 μm thick) served as an interlayer with via openings patterned by photolithography and RIE with O_2. Depositing and patterning a second metal layer (10 nm Cr/500 nm Au) yielded column select lines. Another layer of PI (2 μm thick) encapsulated the second metal layer. A coating Al_2O_3 (20 nm thick, ALD) on the top surface of the PI served as an adhesion

ENGINEERING

promotor for bonding to a sheet of PI (Kapton, 13 μm) coated with Al_2O_3 (20 nm thick, ALD) and laminated on handling substrate (a glass slide coated with PDMS). Here, dispensing a commercial adhesive (Kwik-Sil; World Precision Instruments) between the two Al_2O_3-coated layers of PI layers, applying a pressure of ∼50 kPa, and curing the adhesive at room temperature for 30 min formed a robust mechanical bond. RIE with SF_6/O_2 followed by inductively coupled plasma RIE (Surface Technology System) eliminated the Si substrate to leave the BOX t-SiO_2 exposed on the top surface. Photolithography and etching (RIE with CF_4/O_2 followed by immersion in BOE) removed selected regions of the t-SiO_2 to expose small areas of the p^{++}-Si islands. Thermal evaporation of a bilayer of Cr (10 nm)/Au (300 nm) followed by photolithography and wet etching formed metal pads across the entire area of each unit cell with electrical interface to the electronics on the back side through the p^{++}-Si. Cutting the device with a razor blade along the outer perimeter and peeling it from the handling substrate completed the fabrication process. Application of stiffening layer (Kapton, 150 μm thick) to regions of electrode contacts at the periphery enabled use of a zero insertion force connector as an interface to an external DAQ system.

Methods for Characterizing the Transistors. The following equation defines the effective mobility (μ_{eff}) in the linear regime:

$$\mu_{eff} = \frac{Lg_m}{WC_{OX}V_{DS}},$$

where g_m is the transconductance defined as

$$g_m = \frac{\partial I_{DS}}{\partial V_{GS}},$$

where C_{OX} is the specific capacitance of the gate stack per unit area, and L is effective channel length. C_{OX} can be calculated using the following equation:

$$C_{OX} = \frac{\varepsilon_0 \varepsilon_r}{t_{OX}},$$

where ε_0 is the permittivity of free space (8.854×10^{-14} F/cm), ε_r is the relative permittivity, and t_{OX} is the oxide thickness. For 50 nm SiO_2, $\varepsilon_r = 3.9$. $C_{OX}(SiO_2) = 6.90 \times 10^{-8}$ F/cm^2. For 13 nm Al_2O_3, $\varepsilon_r = 11$, $C_{OX}(Al_2O_3) = 7.50 \times 10^{-7}$ F/cm^2. As a result,

$$C_{OX}(\text{total}) = \frac{1}{\frac{1}{C_{OX}(SiO_2)} + \frac{1}{C_{OX}(Al_2O_3)}} = 6.32 \times 10^{-8} \text{F/cm}^2.$$

Subtracting the phosphorus lateral diffusion length ($2x_d$) associated with thermal oxidation (1,150 °C, 15 min) from the channel length defined by photolithography (20 μm) yields the effective channel length (L_{eff}) of the transistor. The estimated value of x_d is ∼2 μm, and L_{eff} is ∼16 μm. For the transistor shown in Fig. 2*E*, the mobility is estimated to be:

$$\mu_{eff} = \frac{16\mu\text{m} \cdot 2 \times 10^{-5}\text{A/V}}{80\mu\text{m} \cdot 6.32 \times 10^{-8}\text{F/cm}^2 \cdot 0.1\text{V}} = 633 \text{ cm}^2 \cdot \text{V}^{-1} \cdot \text{s}^{-1}.$$

The following equation defines the subthreshold swing (SS):

$$SS = \left(\frac{d(\log I_{DS})}{dV_{GS}}\right)^{-1}.$$

The threshold voltage is the V_{GS} axis intercept of the linear extrapolation of a plot of I_{DS} as a function of V_{GS} at the point of maximum g_m. The value of V_{th} is calculated by subtracting $V_{DS}/2$ from the V_{GS} intercept point to minimize the effects of different values of V_{DS}.

Procedures for Soak Testing the Devices. The soak tests used wells formed with PDMS to confine the PBS over the active areas of the devices. Exposure to UV ozone yielded surface chemistry that enhanced the bonding between the PDMS and t-SiO_2 surface, thereby ensuring a waterproof seal. Thin metal traces deposited by electron-beam evaporation and patterned by lithography and etching provided electrical connections to the device from probe pads located outside of the well. For testing the active matrix system, a glass slide bonded to the back side of the PI substrate with a thin layer of PDMS allowed direct contact to PBS from only the front side. PDMS applied to the peripheral edges minimized the effects of diffusion of water through the PI, the adhesive, and/or the associated interfaces. An oven maintained the entire testing system to set temperatures.

Systems for DAQ. The DAQ system consisted of three PXI-6289 DAQ cards (National Instruments) and a custom acquisition system interface board. The device connected to the DAQ through two flexible high-definition multimedia interface cables and a printed circuit board. Custom LabVIEW software controlled the system by biasing the PBS to simulate the electrical potential generated by biological tissues. An oversampling ratio of 4 further reduced the noise.

ACKNOWLEDGMENTS. We thank the Micro and Nanotechnology Laboratory and the Micro-Nano-Mechanical Systems Laboratory at the University of Illinois at Urbana–Champaign for device fabrication and material characterization. K.J.Y. acknowledges the support from the National Research Foundation of Korea (Grants NRF-2017R1C1B5017728, NRF-2017M1A2A2048880, and NRF-2018M3A7B4071109). L.T. acknowledges the support from Beckman Institute Postdoctoral Fellowship at the University of Illinois at Urbana–Champaign.

1. McKhann GM, 2nd, Schoenfeld-McNeill J, Born DE, Haglund MM, Ojemann GA (2000) Intraoperative hippocampal electrocorticography to predict the extent of hippocampal resection in temporal lobe epilepsy surgery. *J Neurosurg* 93:44–52.
2. Stacey WC, Litt B (2008) Technology insight: Neuroengineering and epilepsy-designing devices for seizure control. *Nat Clin Pract Neurol* 4:190–201.
3. Jeong JW, et al. (2015) Wireless optofluidic systems for programmable in vivo pharmacology and optogenetics. *Cell* 162:662–674.
4. Montgomery KL, et al. (2015) Wirelessly powered, fully internal optogenetics for brain, spinal and peripheral circuits in mice. *Nat Methods* 12:969–974.
5. Kim TI, et al. (2013) Injectable, cellular-scale optoelectronics with applications for wireless optogenetics. *Science* 340:211–216.
6. Canales A, et al. (2015) Multifunctional fibers for simultaneous optical, electrical and chemical interrogation of neural circuits in vivo. *Nat Biotechnol* 33:277–284.
7. Whitmer D, et al. (2012) High frequency deep brain stimulation attenuates subthalamic and cortical rhythms in Parkinson's disease. *Front Hum Neurosci* 6:155.
8. Litt B, et al. (2001) Epileptic seizures may begin hours in advance of clinical onset: A report of five patients. *Neuron* 30:51–64.
9. Viventi J, et al. (2011) Flexible, foldable, actively multiplexed, high-density electrode array for mapping brain activity in vivo. *Nat Neurosci* 14:1599–1605.
10. Khodagholy D, et al. (2015) NeuroGrid: Recording action potentials from the surface of the brain. *Nat Neurosci* 18:310–315.
11. Kim DH, et al. (2010) Dissolvable films of silk fibroin for ultrathin conformal bio-integrated electronics. *Nat Mater* 9:511–517.
12. Xu L, et al. (2014) 3D multifunctional integumentary membranes for spatiotemporal cardiac measurements and stimulation across the entire epicardium. *Nat Commun* 5: 3329.
13. Escabí MA, et al. (2014) A high-density, high-channel count, multiplexed μECoG array for auditory-cortex recordings. *J Neurophysiol* 112:1566–1583.
14. Viventi J, et al. (2010) A conformal, bio-interfaced class of silicon electronics for mapping cardiac electrophysiology. *Sci Transl Med* 2:24ra22.
15. Someya T, et al. (2005) Conformable, flexible, large-area networks of pressure and thermal sensors with organic transistor active matrixes. *Proc Natl Acad Sci USA* 102:12321–12325.
16. Lacour SP, Jones J, Wagner S, Li T, Suo ZG (2005) Stretchable interconnects for elastic electronic surfaces. *Proc IEEE* 93:1459–1467.
17. Tian B, et al. (2010) Three-dimensional, flexible nanoscale field-effect transistors as localized bioprobes. *Science* 329:830–834.
18. Takei K, et al. (2010) Nanowire active-matrix circuitry for low-voltage macroscale artificial skin. *Nat Mater* 9:821–826.
19. Schwartz G, et al. (2013) Flexible polymer transistors with high pressure sensitivity for application in electronic skin and health monitoring. *Nat Commun* 4:1859.
20. Wu W, Wen X, Wang ZL (2013) Taxel-addressable matrix of vertical-nanowire piezotronic transistors for active and adaptive tactile imaging. *Science* 340:952–957.
21. Jeong JW, et al. (2014) Capacitive epidermal electronics for electrically safe, long-term electrophysiological measurements. *Adv Healthc Mater* 3:642–648.
22. Laks MM, Arzbaecher R, Bailey JJ, Geselowitz DB, Berson AS (1996) Recommendations for safe current limits for electrocardiographs. A statement for healthcare professionals from the Committee on Electrocardiography, American Heart Association. *Circulation* 93:837–839.
23. Swerdlow CD, et al. (1999) Cardiovascular collapse caused by electrocardiographically silent 60-Hz intracardiac leakage current. Implications for electrical safety. *Circulation* 99:2559–2564.
24. Bowman L, Meindl JD (1986) The packaging of implantable integrated sensors. *IEEE Trans Biomed Eng* 33:248–255.
25. Liu X, et al. (1999) Stability of the interface between neural tissue and chronically implanted intracortical microelectrodes. *IEEE Trans Rehabil Eng* 7:315–326.
26. Bazaka K, Jacob M (2012) Implantable devices: Issues and challenges. *Electronics* 2: 1–34.
27. Fang H, et al. (2016) Ultrathin, transferred layers of thermally grown silicon dioxide as biofluid barriers for biointegrated flexible electronic systems. *Proc Natl Acad Sci USA* 113:11682–11687.

28. Fang H, et al. (2017) Capacitively coupled arrays of multiplexed flexible silicon transistors for long-term cardiac electrophysiology. *Nat Biomed Eng* 1:1–11.
29. Chi YM, Jung T-P, Cauwenberghs G (2010) Dry-contact and noncontact biopotential electrodes: Methodological review. *IEEE Rev Biomed Eng* 3:106–119.
30. Fairfield JA (2018) Nanostructured materials for neural electrical interfaces. *Adv Func Mater* 28:1701145.
31. Seidel H, Csepregi L, Heuberger A, Baumgartel H (1990) Anisotropic etching of crystalline silicon in alkaline-solutions. *J Electrochem Soc* 137:3626–3632.
32. Tandon N, et al. (2011) Optimization of electrical stimulation parameters for cardiac tissue engineering. *J Tissue Eng Regen Med* 5:e115–e125.
33. Richards DJ, et al. (2016) Nanowires and electrical stimulation synergistically improve functions of hiPSC cardiac spheroids. *Nano Lett* 16:4670–4678.
34. Tybrandt K, et al. (2018) High-density stretchable electrode grids for chronic neural recording. *Adv Mater* 30:e1706520.
35. Tandon N, et al. (2009) Electrical stimulation systems for cardiac tissue engineering. *Nat Protoc* 4:155–173.
36. Santini JT, Jr, Cima MJ, Langer R (1999) A controlled-release microchip. *Nature* 397: 335–338.
37. Frankenthal RP, Siconolfi DJ (1982) The anodic corrosion of gold in concentrated chloride solutions. *J Electrochem Soc* 129:1192–1196.
38. Brummer SB, McHardy J, Turner MJ (1977) Electrical stimulation with Pt electrodes: Trace analysis for dissolved platinum and other dissolved electrochemical products. *Brain Behav Evol* 14:10–22.
39. Merrill DR, Bikson M, Jefferys JG (2005) Electrical stimulation of excitable tissue: Design of efficacious and safe protocols. *J Neurosci Methods* 141:171–198.
40. Qiang Y, et al. (2017) Bilayer nanomesh structures for transparent recording and stimulating microelectrodes. *Adv Funct Mater* 27:1704117.
41. Scholvin J, Fonstad CG, Boyden ES (2017) Scaling models for microfabricated in vivo neural recording technologies. *Eighth International IEEE/EMBS Conference on Neural Engineering (NER)*, eds Tong S, Principe J, Ding L, Sajda P (IEEE, Shanghai, China), pp 181–185.
42. Scholvin J, et al. (2016) Close-packed silicon microelectrodes for scalable spatially oversampled neural recording. *IEEE Trans Biomed Eng* 63:120–130.